Journal of Crystal Growth 360 (2012) 81–86

Contents lists available at SciVerse ScienceDirect

Journal of Crystal Growth

journal homepage: www.elsevier.com/locate/jcrysgro

Characterization of mc-Si directionally solidified in travelling magnetic fields

F.-M. Kiessling [a,*], F. Büllesfeld [b], N. Dropka [a], Ch. Frank-Rotsch [a], M. Müller [c], P. Rudolph [d]

[a] Leibniz-Institut für Kristallzüchtung (IKZ), Max-Born-Str. 2, D-12489 Berlin, Germany
[b] Schott AG, Hattenbergstrasse 10, D-55122 Mainz, Germany
[c] Schott Solar Wafer GmbH, Ilmstrasse 8, D-07743 Jena, Germany
[d] Crystal Technology Consulting (CTC), Helga-Hahnemann-Str. 57, D-12529 Schönefeld, Germany

ARTICLE INFO

Available online 16 March 2012

Keywords:
A1. Directional solidification
A1. Magnetic fields
A1. Impurities
A2. Vertical gradient freeze
B2. Multi-crystalline silicon

ABSTRACT

Solar-grade boron doped silicon has been directionally solidified in a vertical gradient freeze-type furnace equipped with KRIST*MAG*®-heaters to study the influence of travelling magnetic fields (TMFs) on the ingot quality. As-grown silicon ingots of $22 \times 22 \times 13$ cm^3 in volume were cut vertically and analysed. Information was obtained on the curvature of the melt–solid interface, the grain size distribution, the content of SiC and Si_3N_4 particles and the electrical activity of defects. TMFs were used to enhance melt stirring and to control the growth interface shape. Primarily inclusion-free ingots were solidified with grains of several centimetres in size. Minority carrier lifetimes of τ=20–30 μs were measured on polished surfaces of cuts from as-grown ingots. The concentrations of carbon, oxygen and nitrogen were determined by FTIR spectroscopy to $(3–4) \times 10^{17}$ atoms/cm^3, $(2–3) \times 10^{17}$ atoms/cm^3 and $(0.6–2) \times 10^{15}$ atoms/cm^3, respectively. Mean etch pit densities were evaluated on vertical cuts as low as $(2–3) \times 10^3$ cm^{-2}.

1. Introduction

The immense economic price pressure on photovoltaic (PV) modules drives the development of new technologies towards increased yields and efficiencies in the whole value chain. Silicon-based solar cell production dominates the PV market and the key issue is cell efficiency at low costs. The PV market is dominated by two technologies—the Czochralski (Cz) growth of silicon single crystals and the vertical gradient freeze technique (VGF) to produce multi-crystalline silicon (mc-Si). Lower manufacturing cost of mc-Si wafers is very attractive despite the device efficiency of directionally solidified material being lower compared to single crystalline silicon wafers. In the past, the strategy of increasing volumes per crystal solidification process was primarily pursued. Lately, considerable efforts have been made to improve the less favourable crystalline structure of mc-Si with its diverse defects deteriorating the cell efficiency [1–5].

Lattice defects, such as metal impurities, dislocations bundles, grain boundaries, precipitates and inclusions [6–8], are responsible for lifetime limiting recombination processes. A major issue to look at is the presence of oxygen, carbon and nitrogen impurities. For instance it is well known that an increase of oxygen and a decrease of the carbon concentration result in lower dislocation densities [9]. Main sources of the carbon impurity concentrations are the feedstock and the graphite made hot-zone of the furnace, while oxygen may dissolve from the silica crucible. Nitrogen impurities come from the Si_3N_4 coating of the crucible, while e.g. metal impurities may additionally diffuse from the silica crucible. In solid silicon with a sufficiently low metal impurity content, oxygen together with the p-type dopant boron may form undesired metastable BO-related complexes [10] known to limit the carrier lifetime too. It is very important to understand the complexity of all impurity sources and their impact on the material quality. It starts with a proper choice of the growth and post-solidification conditions, e.g. the deflection of the liquid–solid interface. The shape of the growth interface determines the horizontal distributions of foreign atoms in the ingot and the growth direction of grains.

Besides the incorporation of impurities due to their segregation behaviour, a major issue in directional solidification (DS) of silicon is the formation of second phase particles in the melt and their incorporation at the liquid–solid growth interface. The concentrations of carbon and nitrogen in the melt must be kept below their solubility limit; otherwise precipitates of SiC and Si_3N_4 can be formed [11] and be captured at the liquid–solid interface as undesired inclusions. Their incorporation in the crystal is attributed to an overcritical v/G ratio at the crystallisation front or rather morphological instabilities, with v the growth rate and G the temperature gradient. As it is much more difficult to control G, the solidification velocity can be easily

* Corresponding author. Tel.: +49 30 63 92 30 33; fax: +49 30 63 92 30 03.
E-mail address: kiessling@ikz-berlin.de (F.-M. Kiessling).

0022-0248/$ - see front matter © 2012 Elsevier B.V. All rights reserved.
http://dx.doi.org/10.1016/j.jcrysgro.2012.03.017

adapted [12]. For stable growth conditions it is also beneficial, if local temperature fluctuation can be avoided and the thickness of the diffusion boundary layer can be controlled. Furthermore, the shape of the melt–solid interface is a key parameter. Since wafers are cut perpendicular to the solidification direction, a flat interface is beneficial for uniform properties across the wafer. Otherwise, as the sidewalls of the crucible with its coating are sources of undesired nucleation, a slightly convex curved interface is favourable to avoid growth of parasitic grains into the silicon ingot [13].

The temperature regime at elevated temperatures during the solidification process starting with the first solidified part and during post-solidification cooling determines the thermal stress related defect conditions of the material. Temperature and time dependent diffusion processes take place not only inside the ingot, but also from the coated crucible walls into the ingot [14]. Based on a furnace dependent thermal solidification process with a specially designed hot-zone and a proper choice of the post-growth annealing conditions we developed a TMF-assisted growth process. In this paper we present results, which show that the quality of multicrystalline silicon ingots can be improved by applying travelling magnetic fields. Using TMFs, the morphology and shape of the melt–solid interface can be controlled very well via melt flow adjustment.

2. Experimental and numerical approach

2.1. Directional solidification process and material characterization

Fig. 1 shows a photograph of the used furnace and a schematic drawing of the applied growth principle. The furnace has been equipped with KRISTMAG®-heaters [15,16] producing heat and travelling magnetic fields simultaneously. Each of the side-heaters can be operated either only with direct current (DC) or with alternating current (AC) or in a mixed mode with any AC/DC ratio. Heaters at the bottom and top of the crucible were additionally used to generate heat.

Boron-doped solar-grade silicon with a resistivity of about 1–1.6 Ω cm was used. Such p-type doped silicon was melted in silica crucibles coated with silicon nitride, then homogenized and finally directionally solidified. In order to find growth conditions at which constitutional supercooling can be avoided and the deflection of the growth interface can be controlled, different melt flow patterns and temperature distributions were generated by TMFs. The KRISTMAG®-heaters were supplied with a combination of DC and AC, with different AC amplitudes and with different phase shifts among coils at a fixed frequency f of 20 Hz.

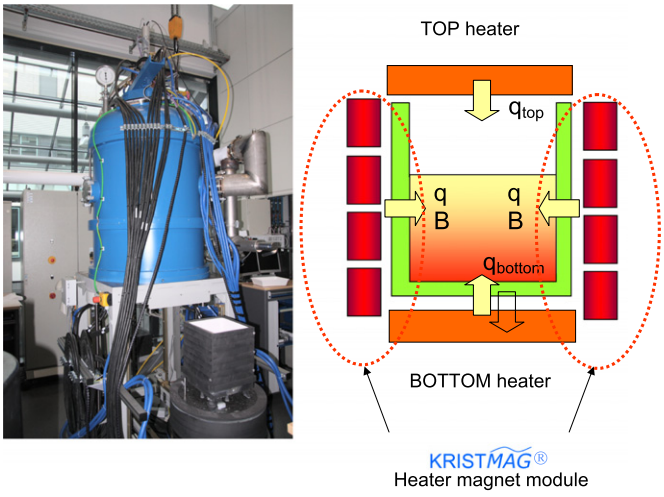

Fig. 1. Photograph of the used furnace and schematic sketch of the DS growth arrangement for Si, showing top and bottom heaters and 4 coils of the side heater to produce TMFs.

Rectangular shaped ingots $22 \times 22 \times 13\ cm^3$ in volume (so-called G1 size) were vertically halved and two slices were cut from each half. For microwave detected photoconductivity decay (μPCD) and Fourier transform infrared (FTIR) spectroscopy measurements surfaces were polished to reduce the influence of surface-related effects. The shape of the liquid–solid growth interface was obtained from striation morphology analysis by lateral photo-voltage scanning (LPS). IR transmission microscopy was used to detect secondary phase particles like SiC and Si_3N_4 inclusions. The grain structure and the mean etch pit density (EPD) were revealed by a KOH-based etchant at 80 °C and a Sirtl etchant at room temperature, respectively. Lifetime measurements were performed by the μPCD method. The content of important system-inherent elements like C, O and N was evaluated from their local vibrational mode absorptions by FTIR spectroscopy measured at wave numbers 605 cm^{-1} (C_s), 1107 cm^{-1} (O_i) and 963 cm^{-1} (NN) using calibration factors of $1.0 \times 10^{17}\ cm^{-2}$ for carbon, $3.14 \times 10^{17}\ cm^{-2}$ for oxygen and $1.83 \times 10^{17}\ cm^{-2}$ for nitrogen [17–19].

2.2. Numerical simulation

Due to lacking geometrical, thermal and flow symmetry, silicon solidification for photovoltaic applications occurring in rectangular melt containers is necessarily a subject of transient 3D studies. Computational fluid dynamics (CFD) and magnetic numerical simulations were performed using the commercial software ANSYS Workbench 2.0. Radiation in the gas phase was described by the discrete transfer method, while gas convection was neglected. The flow patterns in the melt were solved using the $k\omega$-SST turbulence model [20]. In the transient calculations the time step was adjusted to Courant number $Co < 1$. The structured grid for the local melt simulations consisted typically of 5.8×10^6 control volumes with refinement at the walls. Thermal boundary condition resulted from the global calculations for the common furnace configuration. For TMFs driven flow, the Lorentz force density distribution F_L was determined for different parameters. The AC electrical parameters were selected with the aim to provide downwards or upwards directed Lorentz force density fields of different intensity with sufficiently high skin depths.

In a second step, the thermal boundary conditions and body force field obtained in the global calculations were introduced in the local model of the silicon melt motion and the heat transfer. The stirring and interface shaping potential of generated TMFs was appraised using fully developed buoyancy flow field as an initial state and as a benchmark [21].

3. Results and discussions

First of all, a DS process was developed with respect to the furnace possibilities. Fig. 2 depicts a typical as-grown mc-Si ingot, which shows an almost flat last-to-freeze top part. The shape of the top part indicates that the solidification process and the used TMF were properly chosen and a nearly flat growth interface can be assumed. Additionally, one can see that the ingot showed no sticking to the crucible walls at any place. This indicates that a direct contact of liquid silicon with the crucible was prevented and the used Si_3N_4 coating was suitable for the growth process. A sticking-free process is the precondition to obtain crack-free ingots and to avoid strong strain fields responsible for dislocation generation and their multiplication during cooling.

Secondly, in order to control the characteristics of the liquid–solid growth interface via the melt flow, TMF-induced Lorentz

Fig. 2. Image of a standard mc-Si ingot of the size $22 \times 22 \times 13$ cm^3 directionally solidified from solar-grade feedstock.

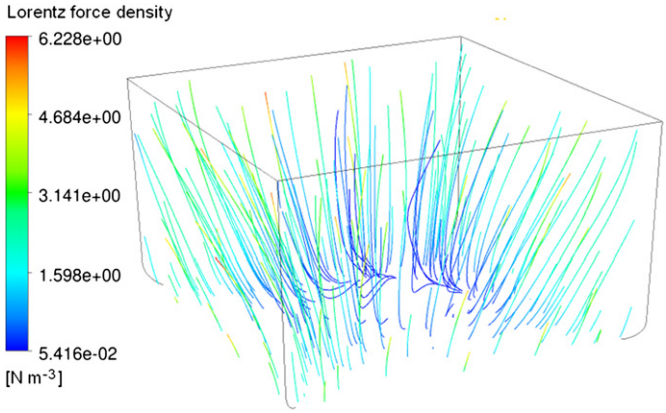

Fig. 3. Image of the Lorentz force density streamlines in a Si melt of G1 geometry calculated for a downward directed TMF with $f=20$ Hz, $\Delta\varphi=-90^\circ$, and $I_{eff}=71$ A (AC).

forces were varied in magnitude and direction. The Lorentz force density distribution can be tuned by all three electrical parameters: frequency ($F_L \sim f^{0.5}$), phase shift $\Delta\varphi$ and AC amplitude ($F_L \sim I_0^2$). An increase in frequency and decrease in phase shift cause the increase in the magnitude of F_L. For diminishing frequencies and a phase shift close to $\pm 90^\circ$ the direction of the Lorentz force density vector becomes more upraised with respect to the crucible bottom. The numerical results showed that Lorentz force densities comparable or larger than the estimated buoyancy force $F_b \approx \rho\beta g\Delta T \approx 7$ N/m^3 were obtained using already moderate electrical currents (Fig. 3). It can be seen that F_L increases towards the crucible walls and has its highest values in the corners. A small frequency of 20 Hz was chosen in order to penetrate sufficiently the melt in our G1 geometry. One has to keep in mind that the skin depth δ_m is proportional to $f^{-0.5}$ and gives, for $f=20$ Hz, $\delta_m=10.3$ cm. If the frequency would be chosen much lower ($f \ll 20$ Hz), the magnitude of AC had to be significantly increased in order to generate F_L in the range of the buoyancy force. Such a change in the AC/DC ratio can be done without any problems as long as it does not affect the power required for the time dependent solidification process, i.e. the maximum amplitude of the alternating current is limited to the process-related used current.

Fig. 4a and b depicts LPS images showing convex and concave curved striations, which correlate to a downward and an upward directed TMF, respectively. In both cases, the TMFs were kept constant during the solidification process, but as expected, the deflection of the revealed liquid–solid interfaces changes due to changing melt flow conditions. These results show that the curvature of the growth interface can be easily controlled. In the case where TMFs are adapted in dependence on decreasing melt height and hence, changing flow conditions, a desired shape can also be kept constant during the whole growth. If horizontal temperature differences responsible for buoyancy forces change with the progress of the crystallization front, Lorentz force density should be adjusted. Numerical simulations have been carried out for such process-adapted TMFs, but have not yet been experimentally verified.

If F_L is of the same order of magnitude as the buoyancy force and it is directed downwards, it can retard the upward flow at the crucible sides, decreasing the velocity in that region. The corresponding temperature profile is then slightly convex and favourable for the growth of high quality crystals. Further increase of F_L brought more symmetry in the flow and a pronounced downward flow along the sidewalls, but generated a too convex temperature profile in the melt (Fig. 4b). The stronger the F_L, the higher gets the maximum velocity in the melt, which is then far above typical DS flow velocities of about $0.1–2 \times 10^{-2}$ m/s [22,23]. The variation in these values is due to furnace-dependent horizontal temperature differences in the melt responsible for the strength of buoyancy forces. We found that weak downwards directed TMFs are beneficial in order to control shape and morphology of the liquid–solid growth interface. The system is then in a transitional flow regime, i.e. neither fully laminar nor fully turbulent.

Besides interface shape control, we tried to determine the solidification velocity. On the same image (Fig. 4b) one can see

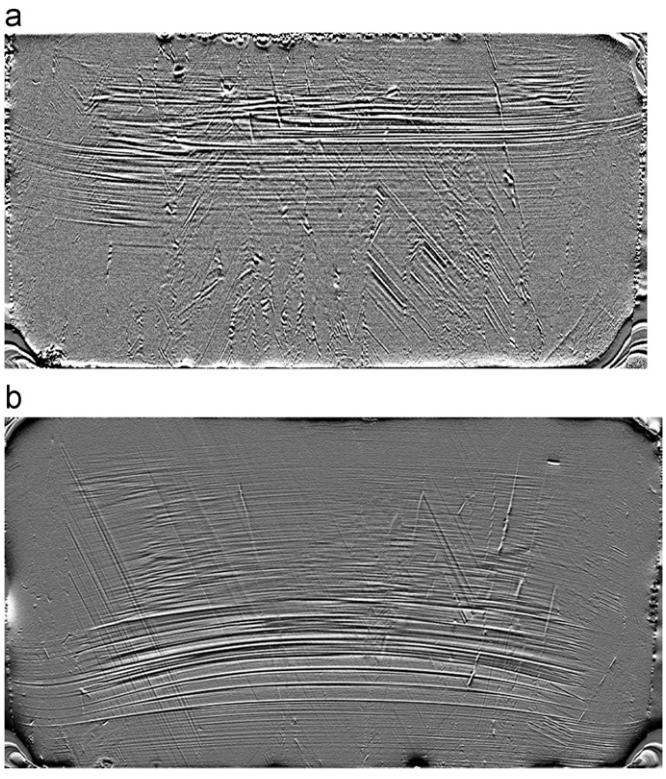

Fig. 4. Images of the liquid–solid growth interface revealed from striation morphology analysis by LPS on vertical cuts: (a) concave curvature at the rim as a result of an applied upward directed TMF: $f=20$ Hz, $\Delta\varphi=90^\circ$, $I_{eff}=35$ A (AC) and (b) convex shape as a result of an applied downward directed TMF: $f=20$ Hz, $\Delta\varphi=-90^\circ$, $I_{eff}=35$ A (AC).

intense striations in the bottom part of the vertical cut caused by periodical changes in the growth velocity. This kind of marker was obtained by tuning the TMF, i.e. the Lorentz force density distribution, in distinct time periods. Frequency and AC amplitude were increased simultaneously within seconds and then tuned back to the growth settings, resulting in a change of the melt flow conditions and finally in fluctuating temperatures at the growth interface. Correlating these striations with the time period between the changes of F_L, the maximum solidification velocity of 1.0 ± 0.1 cm/h was obtained in the middle part of the ingot. At the same growth stage the velocity decreased toward the rims. From these results one can see that the growth velocity differs based on position. In order to get a constant growth velocity at any interface position during the whole solidification process, the applied TMFs have to be fitted to the different growth stages.

A major concern in mc-Si is carbon- and nitrogen-related second phase particles. The initial impurity concentrations of carbon and nitrogen were determined to be 3×10^{17} atoms/cm^3 and 2×10^{16} atoms/cm^3, respectively. These carbon concentrations are typical for CO-enriched conditions [24]. While the nitrogen concentration in the solidified mc-Si was lower by at least one order of magnitude and determined to be $(0.6–2) \times 10^{15}$ atoms/cm^3, carbon was found in similar concentrations. Assuming a carbon solubility limit of about 5×10^{18} atoms/cm^3 [25] and a carbon segregation coefficient $k_0 = 0.07$ [26], one can conclude from the measured concentration in the solidified ingot (Fig. 5) that the melt was additionally contaminated. Unfortunately, besides the furnace hot zone and the crucible, the crucible coating [27] is a source of contamination too. From all parts, mainly carbon, oxygen and nitrogen impurities incorporated in the melt and finally into the ingot. Due to its segregation coefficient $k_0 < 1$ carbon enriches towards the ingot top, but its distribution is additionally influenced by the applied gas regime above the melt. Another evidence of carbon incorporation during the TMF-assisted process can be seen in Fig. 6a. Compared to the standard process (Fig. 6b) an extended process time resulted in a higher carbon concentration in the melt and the formation of SiC precipitates, which can then be found as inclusions at the top of the ingot. Second phase particles were pushed effectively to the ingot top, indicating a morphologically stable growth interface during growth of the inclusion-free ingot part. A similar non-conservative situation is given for oxygen. Although oxygen incorporates into the melt from the crucible, the oxygen concentration decreases in the direction of solidification caused by evaporation and segregation (segregation coefficient $k_0 = 1.4$ [26]).

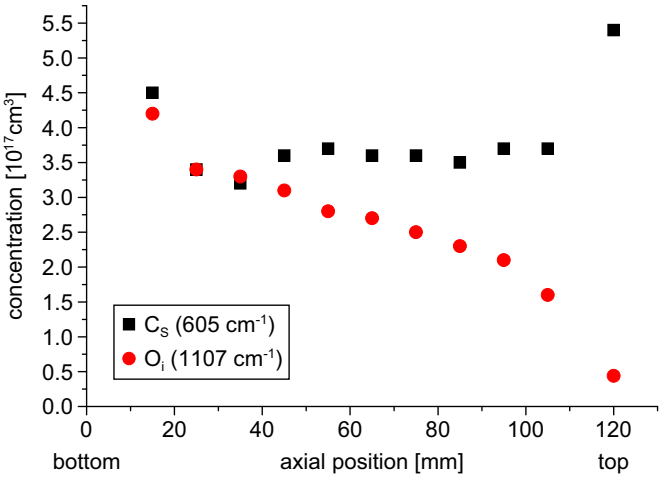

Fig. 5. Typical axial distribution of carbon and oxygen.

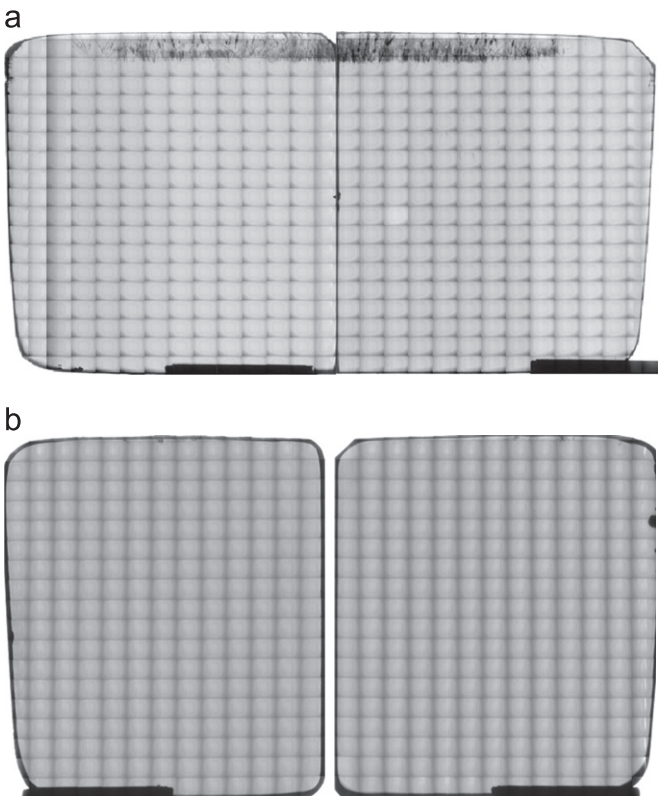

Fig. 6. IR transmission images on vertical cuts: (a) SiC and Si_3N_4 inclusions are found at the top of the ingot based on constitutional supercooling effects of a purposely contaminated melt. (b) By reducing the impurity concentration in the melt, neither SiC clusters or filaments, nor Si_3N_4 rods could be detected.

Even though the concentration of carbon and nitrogen in the melt might have been close to their solubility limit, inclusions were rarely found on vertical cuts of our standard-processed ingots. The ingot cuts were primarily free of second phase particles (Fig. 6b). If at all, very few small inclusions could be detected only at the very last to freeze part of our ingots due to the known continuously increasing carbon concentration with increasing solidification process. We assume that the TMF-induced stirring inhibits the formation of a thick diffusion boundary layer. The increased melt velocity in the vicinity of the liquid–solid growth interface seems to allow an effective rejection of any generated second phase nuclei, in case they were formed. Nevertheless, one has to keep in mind that a high concentration of impurities in the melt will be mirrored in the solid. Their distribution in the ingot depends on diffusion processes induced during ingot cooling. Even nm-sized precipitates might be formed due to the solubility of point defects in the ingot, which create additional strain fields facilitating dislocation formation. Up to now, we did not detect this type of precipitates. Any correlation of precipitation with dislocation formation, which may then form dislocation bundles, has not yet been investigated in our material.

Besides avoidance of second phase particle incorporation at the melt–solid interface and of post-growth precipitation, the cell efficiency can be increased by an improved structural perfection of the material. Since the minority carrier lifetime τ is directly correlated to the cell efficiency, it is an important indicator of the material quality. In order to increase τ, fewer grain boundaries and less or no dislocation bundles are desired. Thus, we tried to improve the grain size in our ingots and developed a TMF-assisted process without seeding. The crucible coating known to affect the nucleation behaviour of grains at the bottom and at the sidewalls was unmodified for all processes. Fig. 7a and b shows images of

the grain structure and its corresponding minority carrier lifetime, respectively, obtained on parallel cuts of one and the same ingot. Grains of several centimetres in size can be seen, which are significantly larger compared with those generally obtained on commercially available wafers from unseeded DS ingots. More details on this process will be published later on [28].

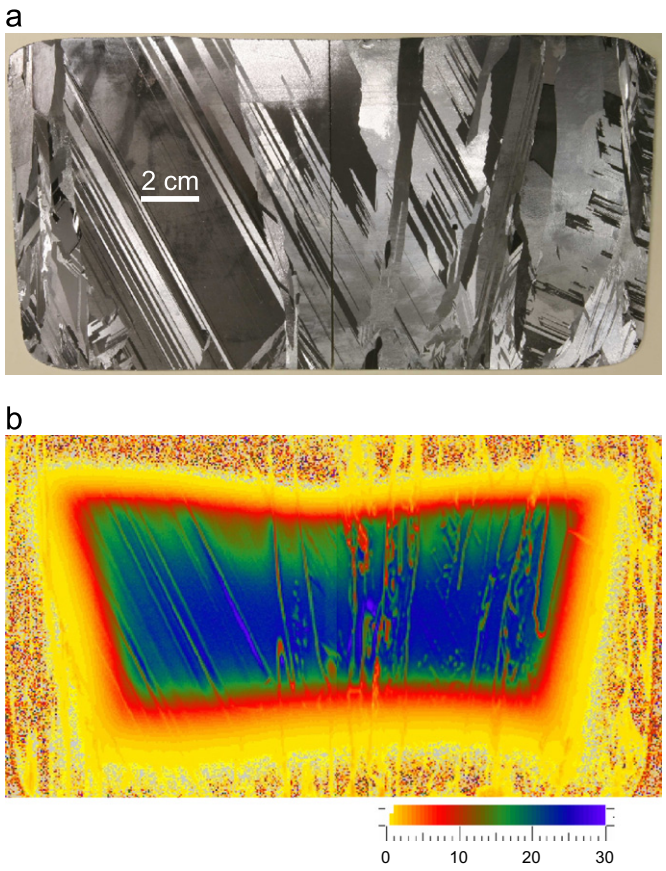

Fig. 7. Images of (a) the grain structure and (b) its corresponding minority carrier lifetime (colour bar in μs) on a vertical cut. (For interpretation of the references to colour in this figure legend, the reader is referred to the web version of this article.)

In Fig. 7b the expected strong correlation of structural defects and lifetime can be seen. Carrier lifetimes of 20–30 μs in large areas of the central part reflect a quite homogeneous distribution of recombination centres. Lower lifetimes mostly correlate with grain boundaries and dislocation bundles. Large grains in mc-Si improve significantly the carrier lifetime. As can be seen in Fig. 7b, slightly lower lifetimes were also measured on twins compared to twin-free single crystalline areas, but it is mostly thought that twin lamellae are electrically inactive [29]. The twin lamellae were predominantly identified as Σ3-type twin boundaries. More investigations are required in order to understand, whether only the defect type or impurities might play a role and cause this activity. The lifetimes decrease also at the rims and the top of the ingot due to the known post-solidification diffusion processes of especially iron [30], but from different sources. Bottom and side parts of the ingot show temperature and time dependent diffusion profiles of metals originated from the crucible and its coating, while the decreased lifetime on top is due to the back diffusion of metal impurities enriched during the growth process due to their very low segregation coefficients.

In order to get an idea of the dislocation distribution, we determined mean EPDs on different grains of the vertical cut shown in Fig. 7a. This ingot is characterized by a twin lamellae-dominated part with large grains and a part with a typical multi-crystalline structure. On the latter, EPDs of $(0.7–2)\times 10^4\,cm^{-2}$ were found in bundle-free areas (see Fig. 8), whereas significantly lower densities of $(2–3)\times 10^3\,cm^{-2}$ were measured on the side with a higher crystalline perfection. The dislocation density is not only highly inhomogeneous from grain to grain, but also differs within the grains. Similar investigation by Bellmann et al. [31] showed significantly higher values. To our knowledge there are only either data measured on wafers or on vertical cuts but we are not aware of data comparing both dislocations densities. The lowest EPDs on wafers we found in literature were about $4\times 10^2\,cm^{-2}$, but varied to higher values by two and more orders of magnitude [32]. For reasons of comparison the EPDs have to be considered with caution, since dislocations densities are dependent on crystallographic directions and higher values seem to be measured on wafers cut parallel to the growth direction. Further intense investigations are required in order to understand grain size growth and to correlate its orientation to the formation of dislocation.

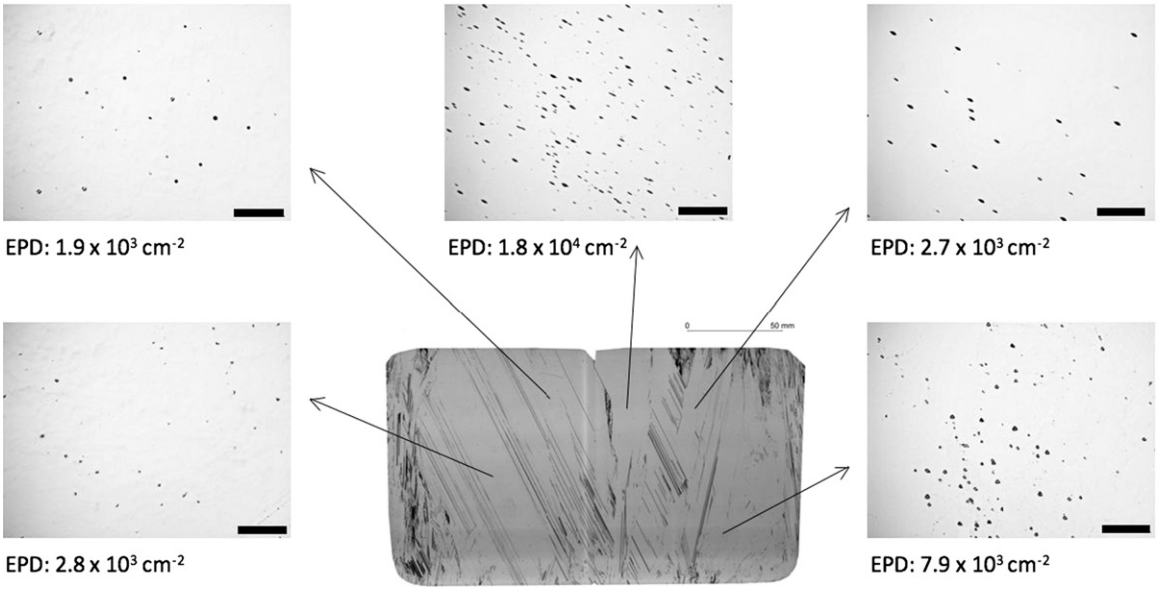

Fig. 8. Images of etched areas on a vertical cut showing mean etch pit densities on different ingot positions within grains. The markers in the EPD pictures correspond to 200 μm.

4. Conclusions

A directional solidification process for multi-crystalline Si was developed in a VGF-type furnace equipped with KRISTMAG®-heaters. Silicon ingots $22 \times 22 \times 13\ cm^3$ in size have been solidified in travelling magnetic fields. We found that TMFs can intentionally be used to influence the melt convection, to reduce the thickness of the diffusion boundary layer and to adjust shape and morphology of the liquid–solid growth interface. We showed that favoured deflections of the interface can be obtained. Almost inclusion-free ingots were solidified with grains of several centimetres in size by a TMF-assisted unseeded process. Within the large grain areas mean EPDs as low as $(2–3) \times 10^3\ cm^{-2}$ were found. Higher and more homogeneously distributed minority carrier lifetimes were measured caused by a reduced number of dislocation bundles. We showed that the application of TMFs together with a proper choice of the growth parameters is a promising tool to improve the material quality of mc-Si. The process optimisation with respect to TMF parameters will be the topic of our further investigations.

Acknowledgements

The authors are grateful to M. Imming and Th. Wurche for ingot preparation, W. Seifert and V. Akhmetov from the IHP/BTU Joint Laboratory in Cottbus, M. Pietsch and M. Naumann for IR measurements, and A. Lüdge for LPS measurements as well as U. Juda and K. Banse for structural characterization. We also thank P. Lange and O. Root for their assisting contributions and K. Irmscher for fruitful discussions.

Partially, this work was supported by the German Federal State of Berlin in the framework of the "Zukunftsfonds Berlin" and the Technology Foundation Innovation Centre Berlin (TSB). It was co-financed by the European Union within the European Regional Development Fund (EFRE).

References

[1] K. Fujiwara, K. Maeda, N. Usami, K. Nakajima, Physical Review Letters 101 (2008) 055503.
[2] N. Stoddard, B. Wu, I. Witting, M.C. Wagener, Y. Park, G.A. Rozgonyi, R. Clark, Solid State Phenomena 131–133 (2008) 1.
[3] I. Takahashi, N. Usami, K. Kutsukake, G. Stokkan, K. Morishita, K. Nakajima, Journal of Crystal Growth 312 (2010) 897.
[4] B. Wu, N. Stoddard, R. Ma, R. Clark, Journal of Crystal Growth 310 (2008) 2178.
[5] H.J. Möller, C. Funke, D. Kreßner-Kiel, S. Würzner, Energy Procedia 3 (2011) 2.
[6] O. Breitenstein, J. Bauer, P.P. Altermatt, K. Ramspeck, Solid State Phenomena 156–158 (2010) 1.
[7] B.L. Sopori, W. Chen, Journal of Crystal Growth 210 (2000) 375.
[8] G. Stokkan, S. Riepe, O. Lohne, W. Warta, Journal of Applied Physics 101 (2007) 053515.
[9] S. Pizzini, et al., Journal of the Electrochemical Society 135 (1988) 155.
[10] K. Bothe, R. Sinton, J. Schmidt, Progress in Photovoltaics: Research and Applications 13 (2005) 287.
[11] H.J. Möller, T. Kaden, S. Scholz, S. Würzner, Applied Physics A: Materials Science and Processing 96 (2009) 207.
[12] M. Trempa, C. Reimann, J. Friedrich, G. Müller, Journal of Crystal Growth 312 (2010) 1517.
[13] F.M. Kiessling, Freiberger Silicon Days, Freiberg, Germany, June 15–17, 2011.
[14] T.U. Nærland, L. Arnberg, A. Holt, Progress in Photovoltaics: Research and Applications 17 (2009) 289.
[15] P. Rudolph, M. Czupalla, N. Dropka, Ch. Frank-Rotsch, F.-M. Kießling, O. Klein, B. Lux, W. Miller, U. Rehse, O. Root, Journal of Korean Crystal Growth and Crystal Technology 19 (2009) 215.
[16] P. Rudolph, Ch. Frank-Rotsch, F.-M. Kiessling, Ch. Kudla, Journal of Ceramic Processing Research 12 (2011) 159.
[17] D. Yang, D. Li, M. Ghosh, H.J. Möller, Physica B: Condensed Matter 344 (2004) 1.
[18] K. Bothe, J. Schmidt, Journal of Applied Physics 99 (2006) 013701.
[19] Y. Itoh, T. Nozaki, Applied Physics Letters 47 (1985) 488.
[20] F.R. Menter, Proceedings of the 24th Fluid Dynamics Conference, July 6–9, AIAA Paper 93-2906, Orlando, Florida, USA, 1993.
[21] N. Dropka, W. Miller, R. Menzel, U. Rehse, Journal of Crystal Growth 312 (2010) 1407.
[22] D. Vizman, J. Friedrich, G. Mueller, Journal of Crystal Growth 303 (2007) 231.
[23] K. Dadzis, J. Ehrig, K. Niemietz, O. Pätzold, U. Wunderwald, J. Friedrich, Journal of Crystal Growth 333 (2011) 7.
[24] L. Raabe, J. Ehrig, S. Würzner, O. Pätzold, M. Stelter, H.J. Möller, Solid State Phenomena 156-156 (2010) 49.
[25] B. Gao, X.J. Chen, S. Nakano, K. Kakimoto, Journal of Crystal Growth 312 (2010) 1572.
[26] M.P. Bellmann, E.A. Meese, L. Arnberg, Journal of Crystal Growth 312 (2010) 3091.
[27] H.C. Starck, Product Description PD-4020 (2009).
[28] F.M. Kiessling, P. Rudolph, N. Dropka, Ch. Frank-Rotsch, Pending Patent DE 10 2011 076 860 (2011).
[29] I. Kuchiwaki, T. Hirabayashi, H. Fukushima, Materials Science Forum 475-479 (2005) 1673.
[30] A.A. Istratov, H. Hieslmair, E.R. Weber, Applied Physics A: Materials Science and Processing 69 (1999) 13.
[31] M.P. Bellmann, T. Kaden, D. Kressner-Kiel, J. Friedl, H.J. Möller, L. Arnberg, Journal of Crystal Growth 325 (2011) 1.
[32] N. Chen, S. Qiu, B. Liu, G. Du, G. Liu, W. Sun, Materials Science in Semiconductor Processing 13 (2010) 276.